Journal of Molecular Structure 1335 (2025) 141866

Contents lists available at ScienceDirect

Journal of Molecular Structure

journal homepage: www.elsevier.com/locate/molstr

Two novel Aroyl Hydrazones from 4-methoxybenzhydrazide: comprehensive study including synthesis, X-ray crystallography, DFT analysis, antibacterial activity and molecular docking

Reshma P . R . [a,b,i], Lincy Tom [c], Dhanya N . P . [d,e], K.P. Safna Hussan [f,g], Vinod P. Raphael [b], V.B. Bhagyesh [h], Bibitha Joseph [a,i,*]

[a] Centre for Research in Chemical Sciences (CRCS), Department of Chemistry, St. Joseph's College (Autonomous), Irinjalakuda, Thrissur 680121, India
[b] Department of Chemistry, Govt. Engineering College, Thrissur 680009, Kerala, India
[c] Department of Chemistry, Nirmala College (Autonomous), Muvattupuzha, Ernakulam, 686661, Kerala, India
[d] Department of Physics, KKTM Govt. College Pullut, Thrissur 680663, Kerala, India
[e] Department of Physics, Christ College (Autonomous), Irinjalakuda, Thrissur 680125, India
[f] Ayurgreen Scientifica Research Institute LLP, Ayurgreen Campus, Kavilpadi, Kaladi, Malappuram - 679 582, Kerala, India
[g] Micro/Nano Technology Centre, Tokai University, Hirastuka-Shi Kanagawa 259-1292,Japan
[h] Department of Chemistry, Christ College (Autonomous), Irinjalakuda, Thrissur 680125, India
[i] University of Calicut, Thenhipalam, Malappuram 673635, Kerala, India

ARTICLE INFO

Keywords:
Aroylhydrazones
4-methoxybenzhydrazide
X-ray crystal structure
DFT
Antibacterial activity
Molecular docking
ADME

ABSTRACT

Two novel aroylhydrazones, 1H-indole-2,3-dione 4-methoxybenzhydrazone (**1**) and 2-(4-chlorobenzoyl)pyridine 4-methoxybenzhydrazone (**2**), were synthesized by reacting 4-methoxybenzhydrazide with equimolar amounts of 1H-indole-2,3-dione and 2-(4-chlorobenzoyl)pyridine. The compounds were completely characterized using single crystal X-ray diffraction, ^{1}HNMR, FT-IR, UV–Vis and elemental analysis. Density functional theory (DFT) calculations at the B3LYP/6311G(d,p) level were employed to optimize their molecular geometries and to analyze their frontier orbitals and charge distributions. Furthermore, the investigated compounds were tested for biological activity against both Gram-positive and Gram-negative bacteria, revealing *in vitro* antibacterial activity. Notably, compounds (**1**) and (**2**) exhibited antibacterial activity solely against the Gram-positive bacterium *Staphylococcus aureus*. To gain structure activity relationship of these compounds docking studies were conducted on four target proteins of *S. aureus*.

1. Introduction

Hydrazone ligands represent a versatile and important class of organic compounds extensively studied in coordination chemistry [1–4]. The structural diversity and tunable properties of hydrazone ligands make them attractive candidates for the synthesis and design of novel metal complexes. Hydrazones and their metal complexes are widely employed in diverse applications in various fields, including catalysis, medicinal chemistry, and analytical chemistry, owing to their capability to form stable chelates with a numerous metal ion and their potential for designing functional materials with tailored properties [5–9]. The biological activities of hydrazones including antimicrobial, anticancer, antitubercular, enzyme inhibition, antioxidant properties, fluorescent probing, drug delivery and antiviral activities, underscoring their potential as versatile compounds in biomedical research and therapeutic development. [10–15]. Furthermore, hydrazones are used as building components in the creation of luminescent materials, which are used in sensors and light-emitting gadgets [16–19]. Hydrazones exhibit notable advantages over imines, particularly in their ease of preparation, tendency to form crystalline structures and enhanced resistance to hydrolysis, making them highly desirable for various applications in coordination chemistry and materials science. Hydrazones possess both nucleophilic and electrophilic characteristics, making them multifaceted compounds in organic chemistry. From a nucleophilic perspective, the nitrogen atom of the hydrazone moiety can act as a lone pair donor, making it prone to attacking electrophilic species. This behaviour allows hydrazones to participate in reactions such as nucleophilic addition to carbonyl compounds, imine formation and

* Corresponding author.
E-mail address: bibitha@stjosephs.edu.in (B. Joseph).

https://doi.org/10.1016/j.molstruc.2025.141866
Received 2 September 2024; Received in revised form 3 February 2025; Accepted 23 February 2025
Available online 24 February 2025
0022-2860/© 2025 Published by Elsevier B.V.

Mannich-type reactions. Conversely, hydrazones can also exhibit electrophilic behaviour. The electron-deficient nature of the carbon atom in the C=N bond makes it susceptible to attack by nucleophiles. This electrophilic character enables hydrazones to undergo reactions such as nucleophilic addition of organometallic reagents, hydrazone functionalization and metal-catalysed transformations. Aroyl hydrazones are a specific class of hydrazones derived from the condensation reaction between an aryl or heteroaryl aldehyde or ketone and a hydrazine or hydrazide compound. These compounds feature an aryl or heteroaryl group directly attached to the C=N bond, imparting distinct electronic and steric properties [20–22]. Their structural versatility allows for modulation of properties such as solubility, lipophilicity and biological activity through appropriate substitution patterns on the aromatic ring [23–26]. If side chains containing donor atoms are absent, aroylhydrazones function as bidentate ligands, where the carbonyl oxygen and the amine nitrogen act as the donor atoms.

By coordinating through multiple donor atoms, aroyl hydrazones can influence the geometry and electronic structure of the metal center, leading to unique properties and potential applications. Extensive antibacterial activity of transition metal complexes is dependent on the complex's shape, the presence of certain type of functional groups, and the composition of the metal ions and ligands. The existence of physiologically significant azomethine functionality makes hydrazone ligands a better option for the production of such complexes. It is possible to create versatile compounds with qualities appropriate for specific uses in many scientific and industrial sectors by modifying their chemical structure.

In the present work, two novel hydrazones were synthesized with a good yield. FT-IR, UV–Vis, ^{1}HNMR, and single crystal X-ray diffraction (XRD) spectroscopy were employed to characterize the molecular structure. Additionally, in order to compare the geometrical and electrical characteristics with the actual data of the compounds under consideration, the Density Functional Theory (DFT) is employed [27–29]. Furthermore, electronic properties such as the Highest Occupied Molecular Orbital (HOMO) and Lowest Unoccupied Molecular Orbital (LUMO, ionization potential (IP), electron affinity (EA), hardness (g), softness (S) and electronegativity (ϖ) were theoretically determined. In the current study, the antibacterial activity of the two hydrazones was investigated with respect to their effects on the pathogenic bacteria *E. coli* and *S. aureus* by well diffusion method. Molecular docking studies with bacterial target proteins were also performed to assess the binding interactions and affinities of the compounds, providing valuable insights into their molecular mechanisms and aiding in the development of potential antimicrobial agent [30–34].

2. Experimental

2.1. Materials and methods

The reagents for synthesis were purchased from Merck, and the solvents were sourced from Aldrich Sigma Ltd. Elemental analyses for carbon, hydrogen, and nitrogen were performed using a Vario EL III elemental analyzer (Elementar). JASCO FT-IR- 4100 Spectrometer was used for recording the IR absorption spectra (4000–400 cm^{-1}) of compounds using KBr pellets. Thermo Scientific Evolution 201 UV–Vis double beam spectrophotometer was used to capture electronic spectra in the 200–800 nm region using 1×10^{-5} M DMF solutions. Proton nuclear magnetic resonance (^{1}H NMR) data was recorded in DMSO with TMS as internal standard using a Bruker Advance III 400 MHz spectrometer with a 9.4 T superconducting magnet.

2.2. Synthesis protocol

Both aroylhydrazones were prepared by adapting a method from a previously published procedure [35].

2.2.1. Synthesis of 1H-Indole-2,3-dione 4-methoxybenzhydrazone (1)

1H-Indole-2,3-dione (0.1471 g, 1 mmol) and 4-methoxybenzhydrazide (0.1661 g, 1 mmol) were mixed in methanolic solutions, which were then refluxed at room temperature for 4 h while being stirred using a Liebig condenser. (Scheme 1). The crystalline orange-coloured precipitate formed was filtered, washed and vacuum-dried over P_4O_{10}. The compound was recrystallized from a mixture of DMF and methanol solution (1:1). The tiny block shaped crystals that apt for single crystal X-ray analysis were separated. (Yield: 84 %; M.P 198 °C)

^{1}HNMR (DMSO-d^6), δ (ppm): 3.82 (s, 3H, OCH_3–), 11.3 (s, 1H, iminol-OH), 6.92–7.85 (m, ArH), 6.98–7.19 (m, 3H, ArH), 7.04 (m, 1H, ArH), 7.12 (m, 1H, ArH), 7.35 (m, 1H Ar-H), 7.58 (m, 1H, Ar-H), 8.04(d 2H) (**Fig. S1)**, CHN calculated for $C_6H_{1\ 3}N_3O_3$ (295.29): C, 65.08 %; H, 4.44 %; N, 14.23 %; O, 16.25 %. Observed: C, 65.05 %; H, 4.45 %; N, 14.21 %; O, 16.23 %.

2.2.2. Synthesis of 2-(4-chloro) benzoyl pyridine 4-methoxybenzhydrazone (2)

A methanolic solution containing 1 mmol of 4-methoxybenzhydrazide (0.1661 g), was added to a methanolic solution of 1 mmol of 2-(4-chloro) benzoyl pyridine and refluxed for 3 h at room temperature with stirring using a Liebig condenser (Scheme 2). Yellow precipitate separated was filtered, washed with methanol and vacuum dried over P_4O_{10}. The compound was recrystallized from a mixture of DMF/methanol solution (1:1). The small diamond shaped crystals obtained after 2–3 days suitable for single crystal X-ray analysis was isolated. (Yield was 82 % and M.P. 173 °C)

^{1}HNMR (DMSO-d^6), δ (ppm): 3.80 (s, 3H, OCH_3–), 7–8.9 (m, ArH), 7.04–7.12 (m, 3H, ArH), 7.32–7.35 (m, 2H, ArH), 7.58 (m, 1H, ArH), 8.04 (m, 2H, ArH). (**Fig. S2)**. CHN calculated for $C_{20}H_{16}ClN_3O_2$ (365.8): C, 65.67 %; H, 4.41 %; Cl, 9.69 %; N, 11.49 %; O, 8.75 %. Observed: C, 65.65 %; H, 4.42 %; Cl, 9.67 %; N, 11.48 %; O, 8.73 %.

2.3. X-ray analysis: data collection, structure determination, and refinement

Crystallographic data were obtained using a Bruker SMART APEX diffractometer with graphite monochromated MoKα (λ = 0.71073 Å) X-ray source. Data acquisition was conducted using Bruker SMART software, and Bruker SAINT Software was employed for data integration. For absorption corrections, SADABS was used, employing Laue symmetry and equivalent reflections. The structure was solved by direct methods using the SHELXL-97 software package and refined on F^2 by full matrix least squares [36]. Non-hydrogen atoms were refined with anisotropic displacement parameters, while hydrogen atoms were located from difference Fourier maps, placed in calculated positions, and refined as riding atoms: C–H = 0.93 Å (heteroaromatic), 0.96 Å (CH_3) and N–H = 0.86–0.87 Å with Uiso(H) = 1.2 Ueq(C,N). With the aid of DFIX and DANG instructions, bond lengths and angles were restrained to maintain proper geometry. Diagrams of all compounds were generated using DIAMOND 3.2 and MERCURY 3.8 programs [37–39].

2.4. Computational methodology

Density functional theory (DFT) was employed for the quantum calculations, which were executed using the Gaussian 09 software package [40]. Initially, the geometry was optimized using the B3LYP/6–311++ G(d, p) level of theory [41]. The B3LYP method integrates Becke's three-parameter hybrid approach, which combines exchange and electronic correlation components within Density Functional Theory (DFT), with the Lee, Yang, and Parr (LYP) correlation functional. The optimized geometry was then utilized for calculating harmonic vibrational frequencies at the B3LYP/6–311++G (d,p) level, ensuring local minima without imaginary vibration frequencies. To achieve a more comprehensive understanding of the aroylhydrazone and its active sites, various quantum chemical analyses were performed,

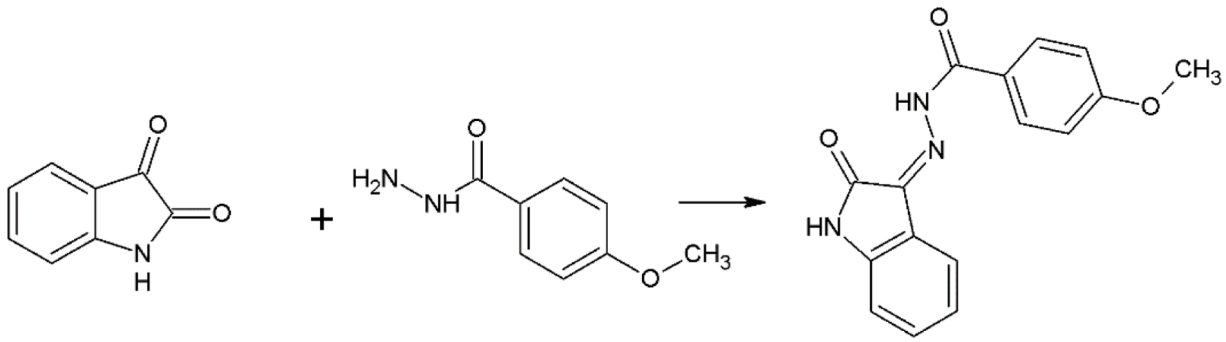

Scheme 1. Synthetic route for 1H-Indole-2,3-dione 4-methoxybenzhydrazone.

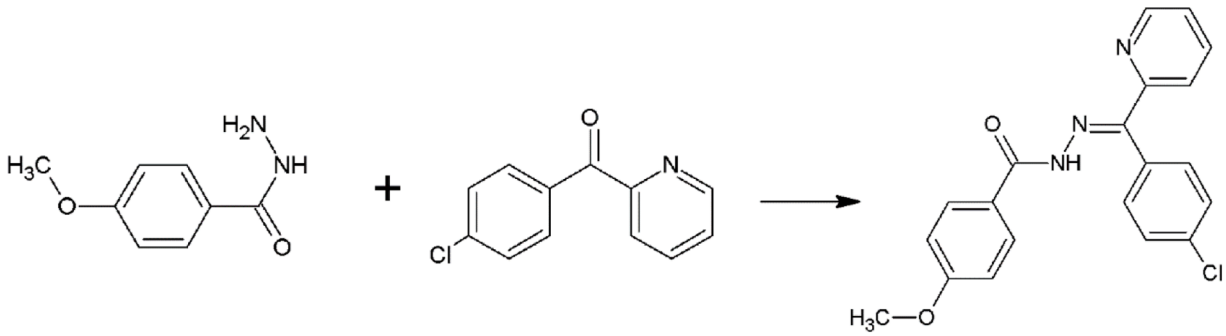

Scheme 2. Synthetic route for 2-(4-chloro) benzoyl pyridine 4-methoxybenzhydrazone.

including bond angles, bond lengths, frontier molecular orbitals (FMO), Mulliken atomic charges, and surface electrostatic potential (MEP) mapping. The chemical reactivity and hardness of the compounds were assessed based on the HOMO and LUMO energies. According to Koopmans' theorem, electron affinity (EA) and ionization potential (IP) have taken as EA = $-E_{LUMO}$ and IP = $-E_{HOMO}$ [42]. The global chemical reactivity descriptors are calculated as follows: electronegativity (χ) = (IP+EA)/2 chemical potential (μ) = – (IP+EA)/2 chemical hardness (η) = (−IP-EA)/2 chemical softness (σ) = 1/2η, electrophilicity index (ω) = $\mu^2/2\ \eta$. Optimized structures, electron densities, molecular orbitals, electrostatic potentials and other surfaces are visualized and analysed through Gauss View [43].

2.5. In-vitro antibacterial studies

The antibacterial activity of the synthesized hydrazones was analyzed using the well diffusion method [44]. 0.1 mL of each bacterial culture (*S. aureus, E.coli*) was uniformly distributed on nutrient agar plates to prepare lawn culture. MHA (Mueller-Hinton agar) plates were prepared and the bacterial culture was spread on the respective plate. Five wells (7mm) were punched and the 100 µl of extract was pipetted to the respective wells and a Gentamicin disc was placed as a positive control. The negative control in the experiment was DMSO. The plates were left to incubate for 24 h, followed by the observation of the zones of inhibition.

2.6. Molecular docking procedure

To provide a detailed explanation for the promising *in vitro* results observed for the hydrazones, a molecular docking study was conducted against four specific target proteins of S.*aureus*. Crystal structure of four proteins of *S. aureus* were collected from RCSB protein data bank (Research Collaboratory for Structural Bioinformatics) with PDB id: 2ZCO, 5IIP, 6FXP and 2BOE. Before docking, existing heteroatoms, ligands and lipids were removed using PyMol 1.3 from the crystal structure [45]. After that hydrogen atoms were added and partial charges were assigned to the selected protein crystal structures. Molecular docking studies were conducted using the SwissDock server, employing a "blind docking" approach against four target proteins. In blind docking, the small molecule is docked to the targets without prior knowledge of the binding site location, allowing for a comprehensive exploration of potential interactions between the molecule and the target. The CIF data found from the single X-ray crystal structure analysis was processed and changed into mol2 format, facilitating the extraction of ligand molecules for subsequent docking studies. During docking analysis, chemical compounds remained flexible, whereas the proteins were allowed to remain rigid. The compounds which were selected acted as reference ligands and proteins acted as targets during the interaction mechanism. Based on the global minimum energy binding, the optimal orientations of the compounds were determined. The detailed assessment of residues related to non-covalent ligand--protein interactions was performed using Accelrys Discovery Studio 4.1, which provided advanced molecular modelling and structural analysis capabilities [46].

3. Results and discussions

3.1. X-ray diffraction analysis

The single crystals of **1** and **2** appropriate for X-ray diffraction analysis were obtained by allowing a DMF/methanol solution to evaporate slowly. **1** and **2** were solved in non-centrosymmetric polar monoclinic crystal system with space group Cc for **1** and P21/n for **2** with four molecules per unit cell. Figs. 1 and 2 show the molecular structure and Table 1 represents the crystallographic details of compound **1** and **2**.

The crystal structures were examined to investigate the role of intermolecular and intramolecular interactions in the stability of compounds **1** and **2**. The overlay of the structures **1** and **2** is shown in Fig. 3. It is evident that they exhibit almost identical conformations along the

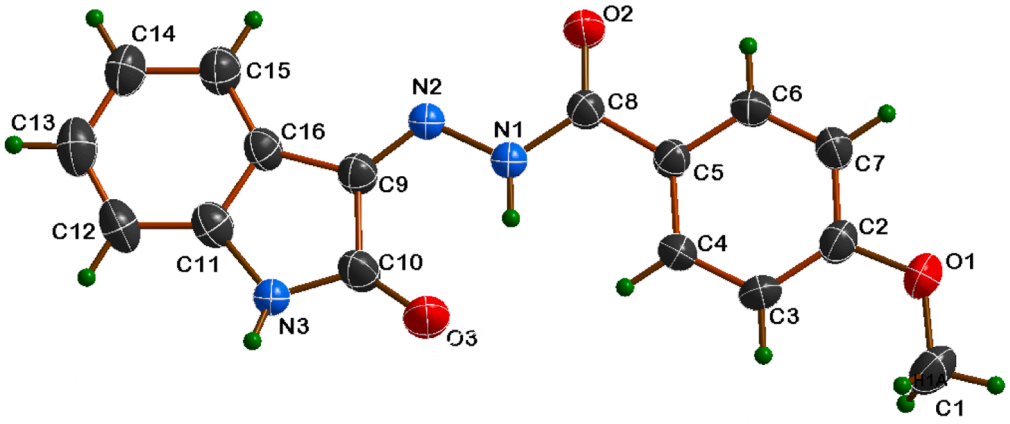

Fig. 1. Asymmetric unit of compound 1.

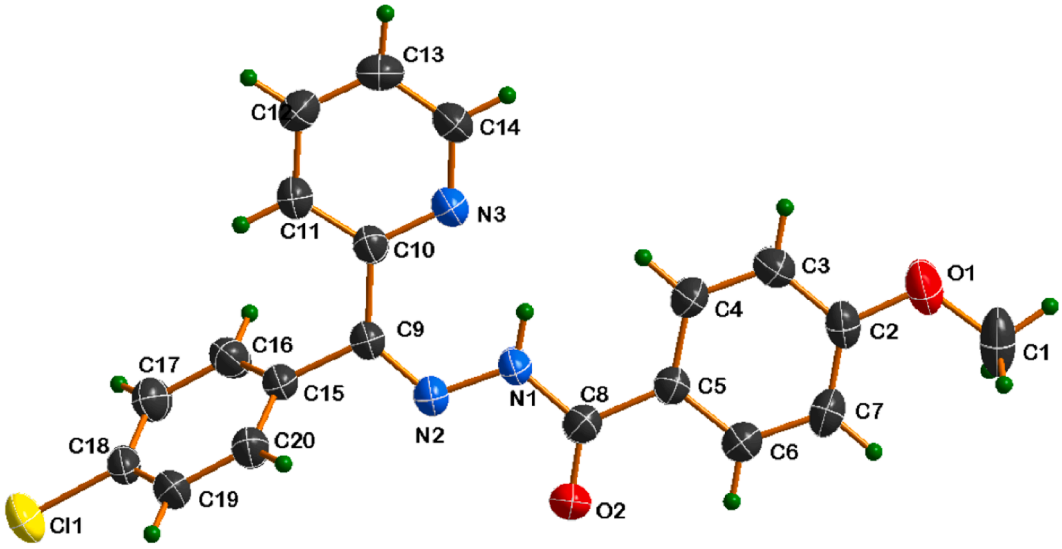

Fig. 2. Asymmetric unit of compound 2.

Table 1
Crystal and structure refinement data for compounds 1 and 2.

Empirical formula	$C_{16}H_{13}N_3O_3$ (1)	$C_{20}H_{16}ClN_3O_2$ (2)
Formula weight	295.29	365.81
Temperature	296(2) K	296(2) K
Wavelength	0.71073 Å	0.71073 Å
Space group	*Cc*	*P21/n*
Crystal system	Monoclinic	Monoclinic
Unit cell dimensions	a = 12.878(4) Å b = 15.821(4) Å c = 6.9568(15) Å β =102.650°	a = 7.2485(9) Å b = 12.5132(12) Å c = 19.333(2) Å β = 91.000(5)°
Volume	1382.9(6) $Å^3$	1753.2(3) $Å^3$
Z	4	4
Density (calculated)	1.418 mg/m^3	1.386 mg/m^3
Absorption coefficient	0.10 $1mm^{-1}$	0.238 mm^{-1}
F(000)	616	760
Reflections collected	8255	13,404
Independent reflections	3285 [R(int)= 0.0419]	3937 [R(int) = 0.0468]
Goodness-of-fit on F^2	0.970	0.978
Data / restraints / parameters	3285/4/209	3937/ 0/236
Final R indices [*I* > 2sigma (I)]	R_1=0.0496, wR_2=0.1218	R_1=0.0481, wR_2=0.1165

hydrazide fragment. The hydrazide nitrogens (N1 and N2), carbonyl oxygen (O2) align in the same direction in both structures. However, for **1** the methoxy group is differently twisted with respect to C2–O1 with a torsion angle (C1–O1–C2–C3) of 173.79°, which is equal to 1.36 for **2**.

The supramolecular structure fragments of are shown in Figs. 4 and 5. Investigation of the crystal packing indicated that compounds **1** and **2** form different supramolecular networks, a discrepancy caused by the influence of their distinct intermolecular interactions in the lattice. The formation of one-dimensional and two-dimensional supramolecular structures in compound **1** and **2** can be analysed in terms of intermolecular and intramolecular hydrogen bonding motifs. The one-dimensional supramolecular structure in compound **1** contains intermolecular N(3)–H(3)···O(2) and intramolecular N(1)–H(1)···O(3) hydrogen bonds running parallel to the 'a' axis. The interaction of indole nitrogen (N3) and O2 of hydrazine moiety is responsible for the propagation of 1D chain in compound **1**. In **2** the Cl atom engages in two intermolecular C(3)–H(3)···Cl(1) and C(14)–H(14)···Cl(1) hydrogen bonds. The interaction of oxygen atom (O2) with neighbouring aromatic ring C(19)–H(19)···O(2) extend the propagation of chain to infinite 2D architecture. Hydrogen bonding parameters are shown in **Table S1**.

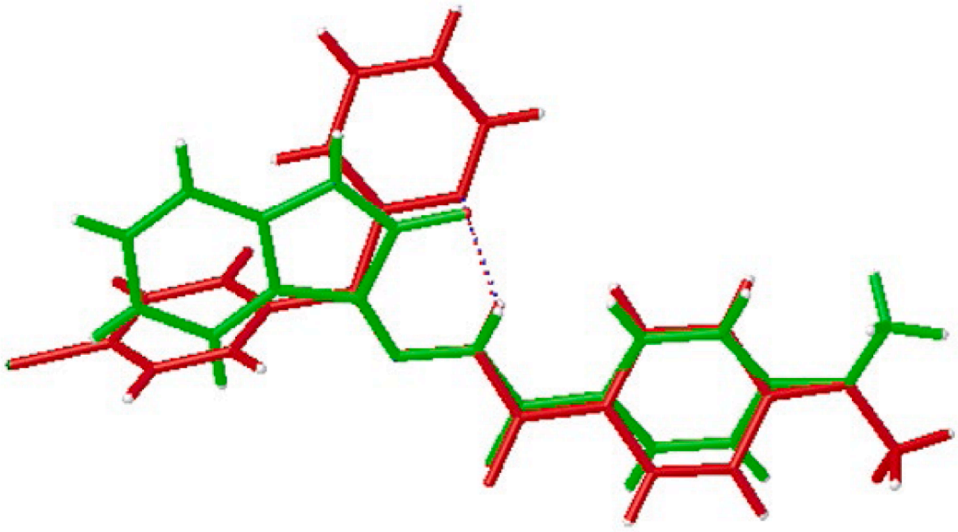

Fig. 3. The overlay structure of 1 and 2.

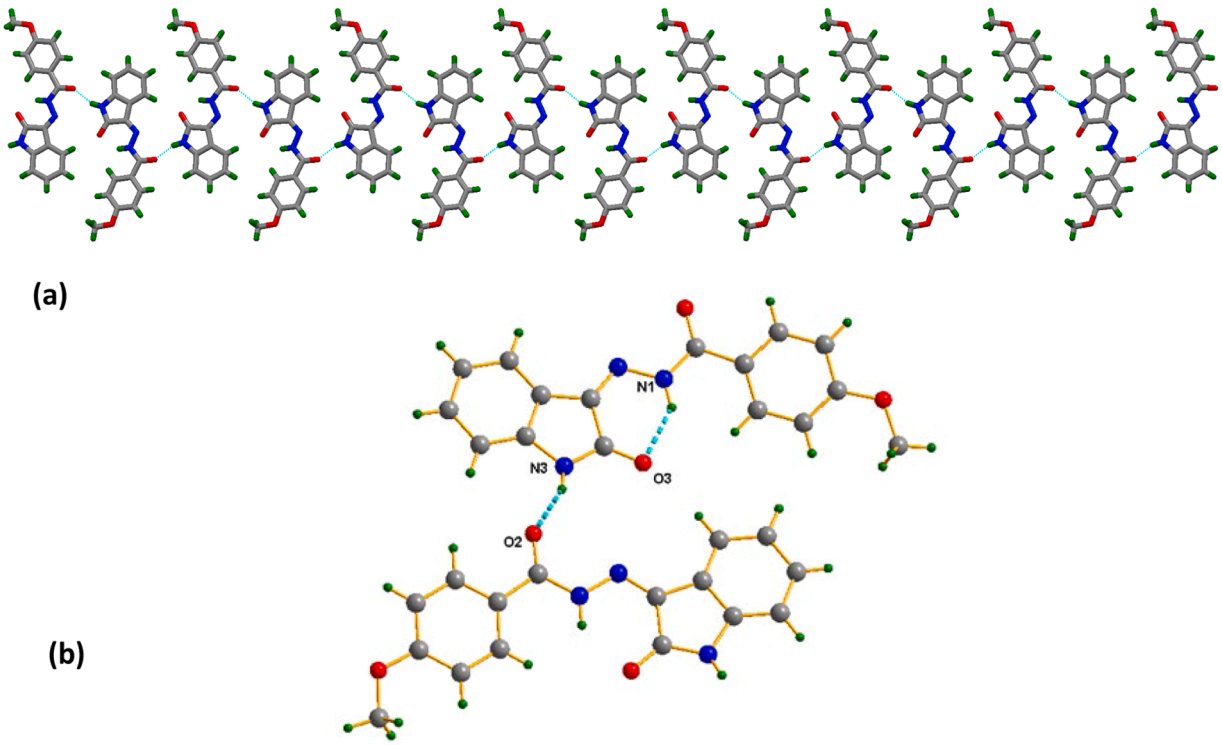

Fig. 4. (a) A view of the 1D supramolecular architecture in compound 1 extending in the ab plane (b) Intermolecular and intramolecular hydrogen bonding interactions of compound 1.

3.2. Computational analysis

3.2.1. Optimized molecular structure

The geometries of the compounds were optimized using density functional theory to get more information on the molecular and electronic structures. The confirmed converged geometry, which signifies that the structure is at a true energy minimum, was validated by the absence of imaginary frequencies during the vibration mode calculation, indicating that the structure is in a stable state and confirming that it represents a true equilibrium configuration, as imaginary frequencies would otherwise suggest potential energy barriers or instability. The optimized geometries are depicted in Figs. 6 and 7. The lowest energy geometric configuration of compound **1** differs from the configuration observed in the crystalline structure. It is expected that the compound adopts a different configuration in the gaseous state compared to the crystalline structure due to the influence of intermolecular and intramolecular hydrogen bonding interactions. The geometry has changed from E configuration to Z configuration in gaseous state. The overlay structure of optimized geometry and crystal structure of compound is given in Fig. 8. Notably, the methoxybenzhydrazide moiety remains largely unchanged, while the rest of the molecule undergoes considerable alterations in both configuration and conformation. These

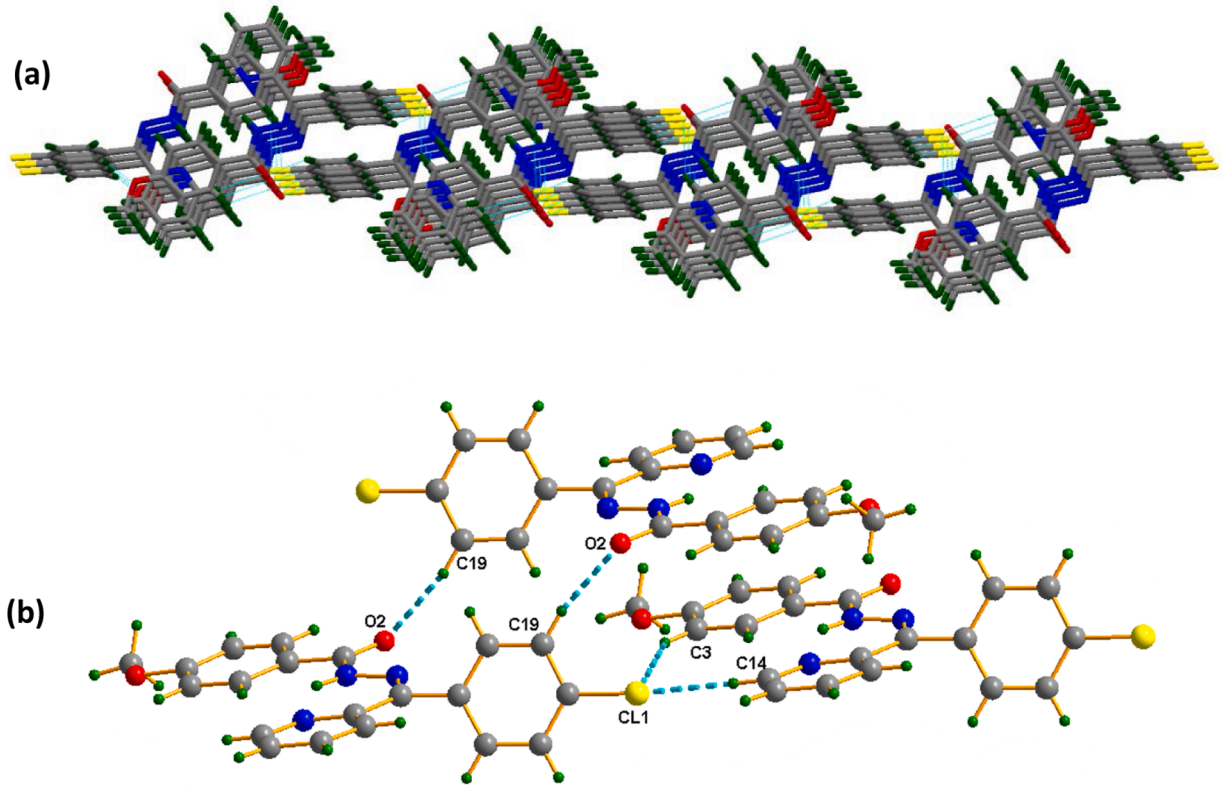

Fig. 5. (a) A view of the 2D supramolecular architecture in compound 2 extending in the ab plane (b) Hydrogen bonding interactions between neighbouring molecules.

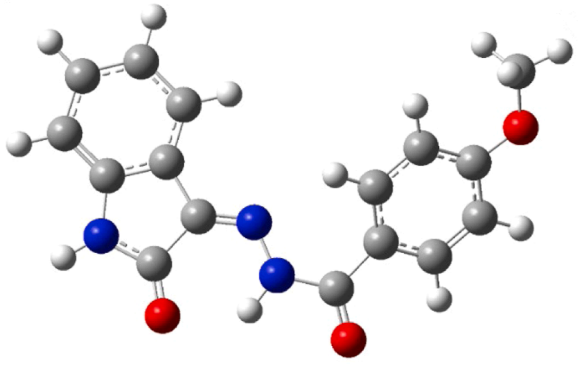

Fig. 6. Optimised structure of compound 1.

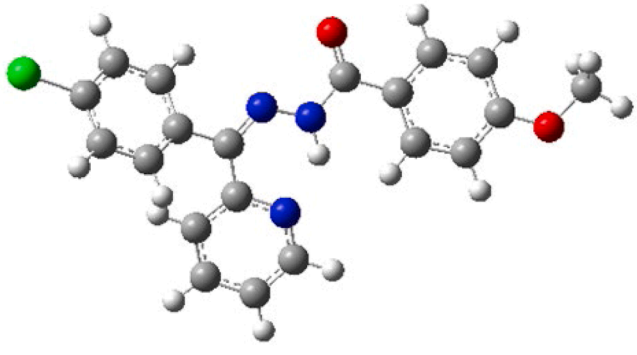

Fig. 7. Optimised structure of compound 2.

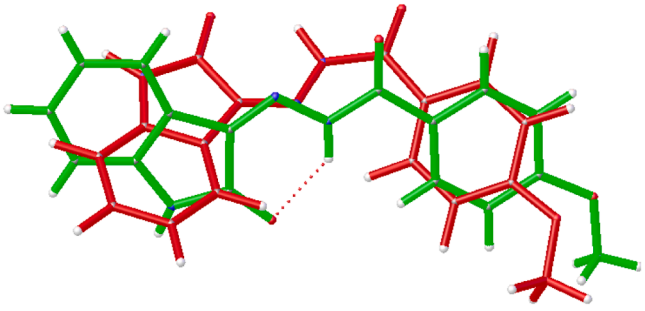

Fig. 8. Structure overlay diagram of compound 1 (crystal structure is shown in green colour and optimized geometry is represented in red colour).

differences likely arise from the absence of crystal packing forces and intermolecular interactions during the optimization process, allowing the molecule to adopt its energetically preferred gas-phase structure. The geometry of the optimized compound **2** differed very little from the original crystallographic conformations. A comparison was made between experimental and theoretical data and prominent bond lengths and bond angles (XRD and DFT) values for compound **1** and **2** are listed in **Table S2** and **S3**. The geometrical parameters match those derived from X-ray diffraction measurements. XRD/DFT histogram of bond lengths and bond angles for compounds **1** and **2** is given in Fig. 9.

3.2.2. Electronic properties and frontier molecular orbitals (FMO) analysis

The frontier molecular orbitals of both compounds were analyzed to gain insights into their electronic transitions, reactivity, and optical properties. The energy gap between MOs plays a crucial role in a molecule's electron transport capability. A smaller frontier orbital gap

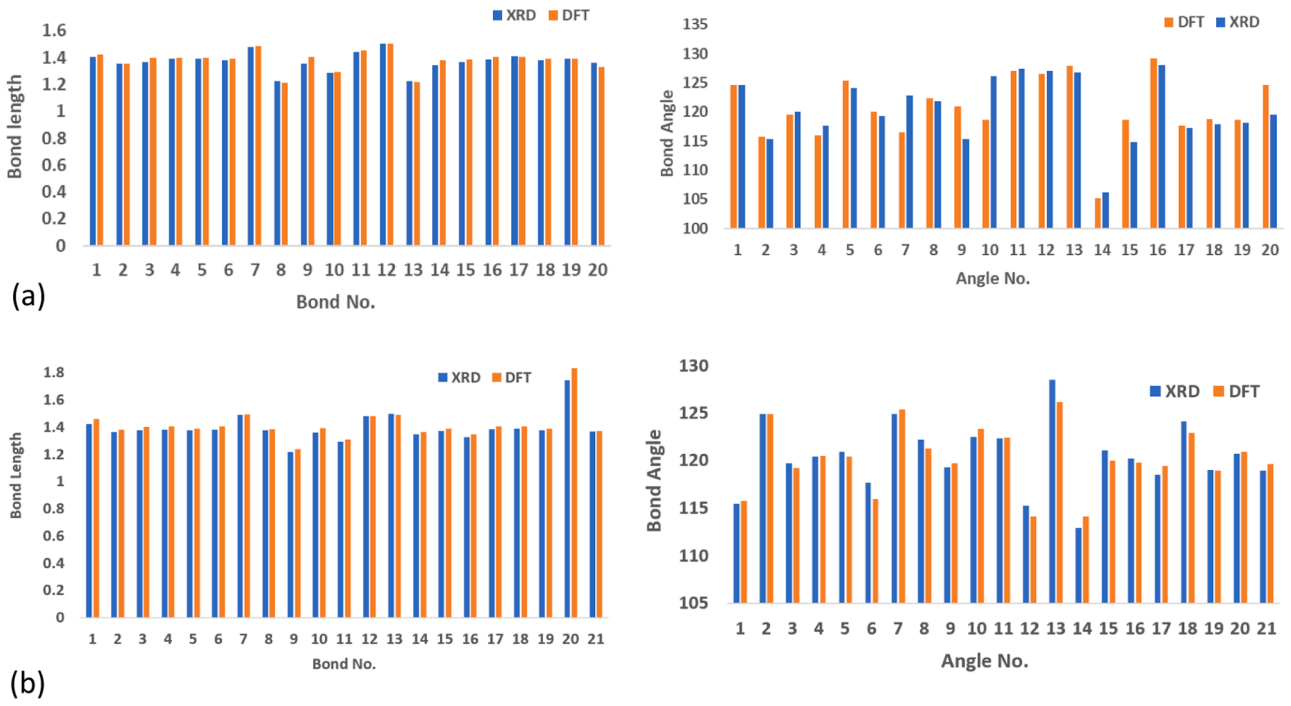

Fig. 9. XRD/DFT histogram of bond lengths and bond angles for compound 1(a) and 2 (b).

indicates high reactivity with low kinetic stability and is also referred to as soft molecule. A smaller frontier orbital gap suggests higher reactivity and lower kinetic stability, characterizing the molecule as "soft." Conversely, a larger orbital energy gap denotes greater chemical hardness, stability, and reduced reactivity. Chemical hardness refers to a compound's resistance to changes in its electron number [47]. The 3D plots of the frontier orbitals, HOMO and LUMO for the compounds **1** and 2 are shown in Fig. 10. The calculated HOMO and LUMO energies, electro negativity (χ), chemical hardness (η), electron affinity (EA), chemical potential (μ), ionization potential (IP) and total energy for title compounds have been summarized in Table 2.

In molecular interactions, the LUMO act as an electron acceptor and its energy corresponds to the electron affinity (EA). Conversely, the HOMO serves as an electron donor and its energy is associated with the ionization potential (IP). Hence, according to Koopmans theorem, electron affinity (A) and Ionization potential (I) can be calculated as negative energies of HOMO and LUMO respectively [42]. Since the compound with high HOMO-LUMO energy gap are stable and chemically harder, it is evident from Table 2 that compound **2** has higher hardness and stability (less reactivity) compared to compound **1**. The chemical potential and electronegativity (χ) exhibit antagonistic features. Compounds with higher chemical potential values tend to be more

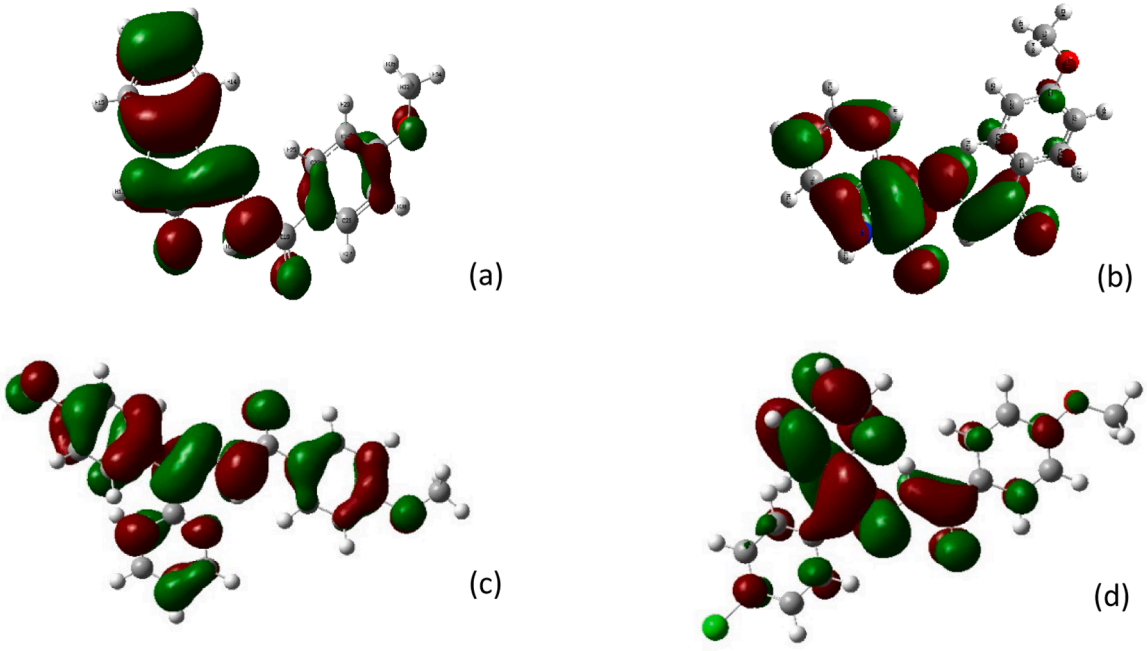

Fig. 10. HOMO (a) and LUMO (b) of Compound 1, HOMO (c) and LUMO (d) of Compound 2.

Table 2
Calculated electronic parameters of the two compounds using DFT/B3LYP/6311Gdp level of theory.

Electronic Parameter	Calculated value	
	Compound 1	Compound 2
E HOMO (eV)	−6.23	−7.14
E LUMO (eV)	−2.48	−1.06
Band Gap Energy (eV)	3.75	6.08
Ionization potential (IP)	6.23	7.14
Electron affinity (EA)	2.48	1.06
Hardnes (η)	1.87	3.04
Softness (S)	0.27	0.16
Electronegativity (χ)	4.35	4.10
Chemical potential (μ)	−4.35	−4.10
Electrophilicity index (ω)	5.06	2.76

reactive, while electronegativity (χ) reflects a compound's tendency to attract electrons. The electrophilicity index (ω) assesses a compound's electrophilic characteristics, providing insights into its potential reactivity and interactions, and is particularly valuable for predicting the compound's toxicity and biological activity [48,49]. Based on electrophilicity index organic compounds are categorised into marginal ($\omega < 0.8$ eV), moderate ($0.8 < \omega < 1.5$ eV) and strong electrophiles ($\omega > 1.5$ eV). Consequently, compound **1** and **2** are strong electrophiles. It is clear that the high electrophilicity (5.06 eV) and small chemical hardness (1.87 eV) correspond to high absolute value of chemical potential (4.35 eV) for compound **1** thereby, suggesting more biological activities for compound **1** compared to **2**.

The HOMO-LUMO energy gap of compound **1** and **2** are 3.75 eV and 6.08 eV, respectively. The energy gap value corresponds to the minimum energy needed for electronic excitation, primarily linked to the π-π* transition [50]. In compound **1**, the isodensities in HOMO is mainly focused over both indole and benzhydrazone moieties; conversely the LUMO is projected over indole moiety and hydrazone group only. Similarly in the HOMO of the compound **2** the isodensities are localised on both benzoyl pyridine and hydrazone moiety. Whereas, LUMO is localized only on pyridine ring and hydrazone group. This suggests that the hydrazone group and both rings in the compounds could act as electron donors. However, in compound **1**, the hydrazone group along with the indole ring, and in compound **2**, the hydrazone group along with the pyridine ring, primarily function as electron acceptors due to their nucleophilic and electrophilic characteristics, respectively.

3.2.3. Molecular electrostatic potential (MEP) Mulliken atomic charges population analysis

MEP characterizes a molecule's charge distribution, hydrogen bonding sites, and regions susceptible to electrophilic and nucleophilic reactions, making it useful for predicting chemically active sites within the molecule [50]. The colour scheme used to represent the MEP of compounds **1** and **2** ranges from deepest red (indicating maximum electron concentration, nucleophilic sites) to deepest blue (indicating maximum electron deficiency, electrophilic sites). The dispersion of potential in compound **1** range from −8.029 e-2 to 8.029 e-2, and where as in compound **2** is −6.838 e-2 to 6.838 e-2. The MEP calculation surface of the compounds is shown in Fig. 11. The presence of negative charge density on N1, O3 in compound **1** and N2, O3, N3 in compound **2** made these sites electron rich and capable for metal binding.

Mulliken population analysis was performed to estimate the partial atomic charges, revealing atoms with nucleophilic and electrophilic properties. As shown in **Fig. S3**, all nitrogen and oxygen atoms exhibit negative Mulliken charges. Additionally, all carbon atoms carry a negative charge, except for those directly bonded to nitrogen and oxygen atoms. Even though all hydrogen atoms are electropositive, hydrogen atoms attached to nitrogen have high electrophilic character indicating its ability to form H-bonds in the solid state.

3.2.4. FT-IR and electronic spectral analysis

Optimized structure parameters are used to find the vibrational frequencies of the compounds. After scaling the wavenumbers with a scaling factor of 0.99 the experimental and theoretical were observed to be in excellent agreement with each other and is shown in Fig. 12**a** and **b** [51]. The minor variations between the experimental and theoretical outcomes are attributed to the experimental data being obtained in the solid phase, in contrast to the theoretical results derived for the gas phase. The spectra were analyzed in the 4000 to 400 cm^{-1} range to confirm the anticipated structure and assess the vibrational frequencies of the characteristic groups. The important bands and their tentative assignments are detailed in Table 3. It is observed that a good agreement has been obtained between the experimental spectrum and theoretical one developed using TD-SCF DFT-B3LYP/6–311 G(d,p).

Assignment of the absorption bands was performed according to literature and the results of theoretical study [52]. Hydrogen-bonding interactions cause notable changes in the infrared (IR) spectrum, such as frequency shifts and increased IR intensity for vibrational bands associated with the functional groups directly involved in the hydrogen bonds. The vibrations of the NH group are likely to be the highly sensitive, exhibiting significant shifts in the spectra due to hydrogen-bonding. For the investigated hydrazones **1** and **2,** the observed symmetric stretching vibrations of NH are located at 3185 and 3317 cm^{-1}. The calculated N—H stretching vibrations are at 3566, 3340 cm^{-1} and 3471 cm^{-1} respectively in **1** and **2** [53]. The frequency at 3317 cm^{-1} in **2** is not H-bonded and very weak. Large frequency shift in NH

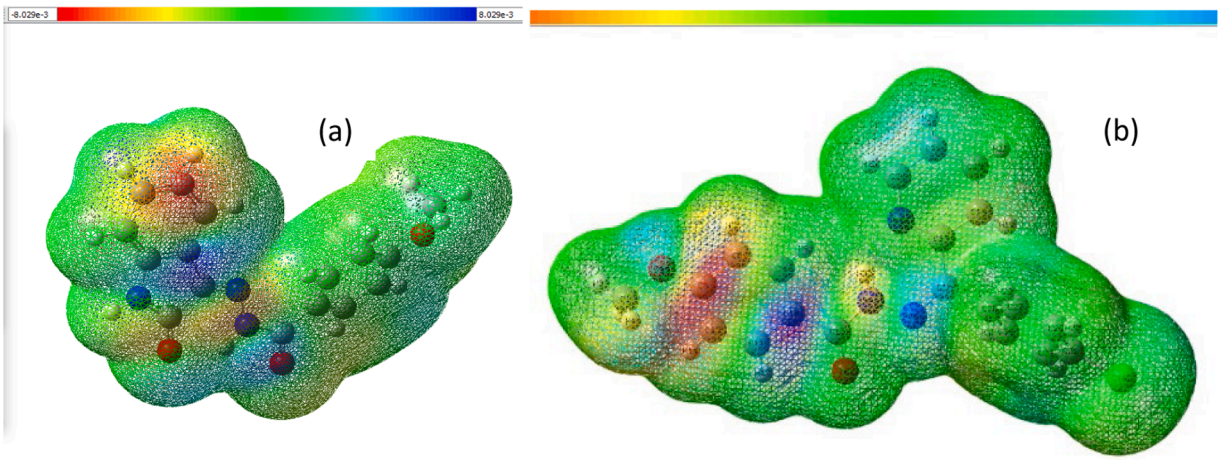

Fig. 11. MEP (Molecular Electrostatic Potential Map) of compound 1(a) and 2 (b).

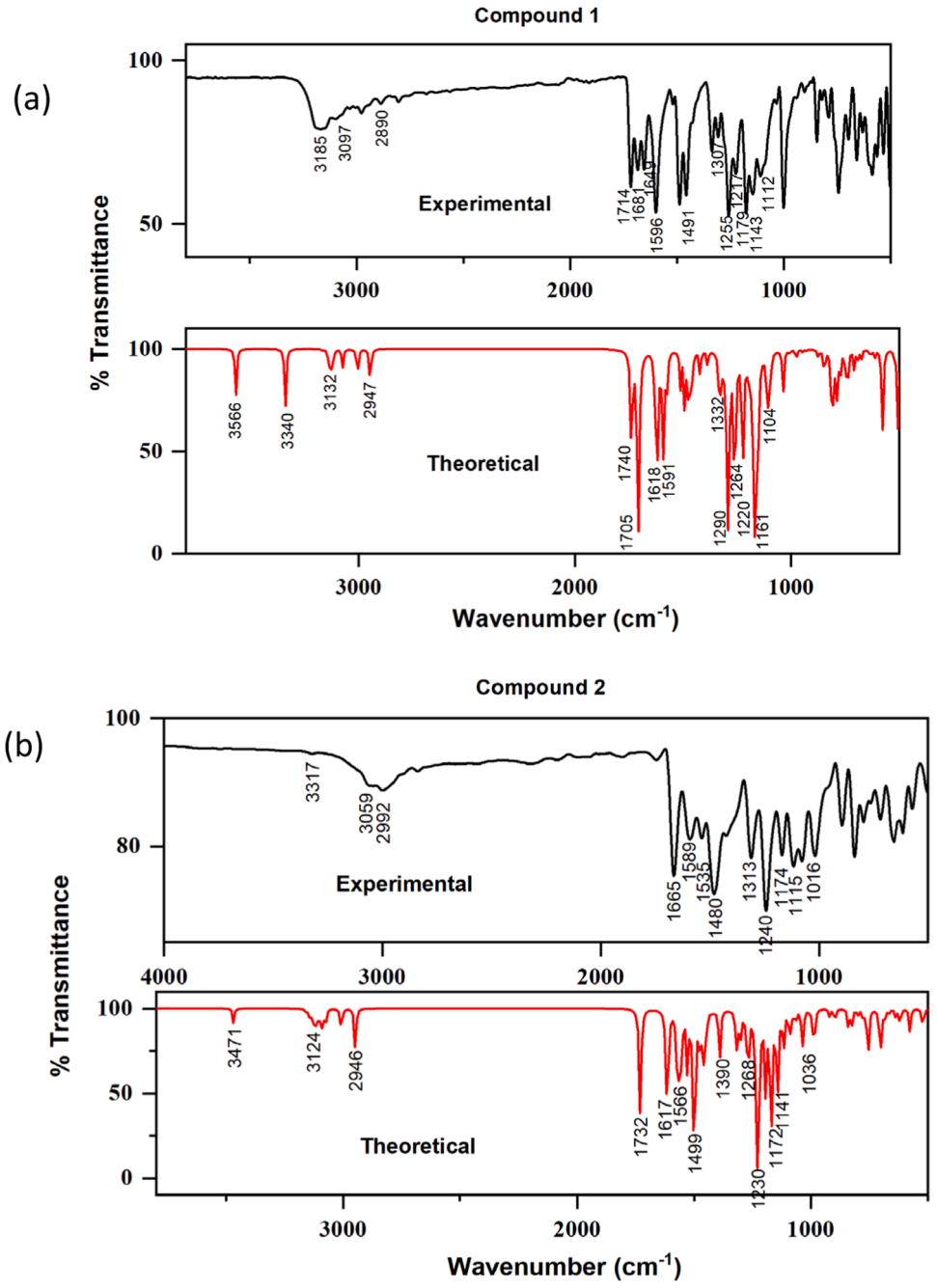

Fig. 12. Theoretical and experimental FT-IR spectra of compound 1 and 2.

stretching vibration suggests the existence of strong intramolecular and intermolecular hydrogen bonds between molecules in compound **1**. The overlap of bands due to hydrogen bonding interactions leads to a single peak corresponding to NH band in compound **1**. Aromatic C—H stretching vibrations are observed as broad bands above 3000 cm^{-1}. The experimental values are well coinciding with the theoretical scaled values [54,55]. The bands in the region of 1680–1735 cm^{-1} are due to C=O stretching vibrations. The large shift in wavenumbers compared to calculated data is caused by the presence of a strong hydrogen bonding in both compounds. The hydrazones exhibit their characteristics azomethine bands (>C=N–) at frequencies 1649 and 1589 cm^{-1} for compound **1** and **2** respectively indicating that condensation between hydrazide and carbonyl compound has resulted in the formation of desired hydrazone. C=N stretching vibrations also correlated excellently between theory and experiment. Similarly, the computed aromatic C=C vibrations showed very nice agreement between theory and experiment. The bands appearing in the spectrum at 1307,1255, 1313 and 1240 cm^{-1} correspond to the stretching vibrations of the C–O groups. The calculated bands were found at 1332,1290, 1268 and1230 cm^{-1}. N–N and C–N stretching modes for both compounds show also a good agreement with the theoretical results. The CH out-of-plane and in-plane bending vibrations appear in the range of 750–1000 cm^{-1} respectively in compound **1** and **2** [56]. From these observations it can be inferred that both hydrazones exist as amido form in the solid state.

The experimental absorption behaviour and TD-SCF DFT-B3LYP/6–311 G(d,p) computation were conducted in DMF solvent and shown in Fig. 13. Compound **1** exhibits absorption bands at 353 nm, and Compound **2** shows bands at 342 nm, which are linked to $\pi \rightarrow \pi^*$ and $n \rightarrow \pi^*$ transitions involving the carbonyl groups, benzene rings, and imine structures in hydrazones. he theoretical predictions indicate that

Table 3
Theoretical and experimental FT-IR spectral data of compound 1 and 2.

Assignments	Compound 1 (cm^{-1})		Compound 2 (cm^{-1})	
	Exp	**Cal**	**Exp**	**Cal**
N-H stretching	3185	3566, 3340	3317	3471
C-H aromatic stretching	3097	3132, 3070, 3004	3059	3117,3124, 3073,3011
C-H aliphatic stretching	2890	2947	2949	2992
C=O stretching	1714, 1681	1740,1705	1665	1732
C=N stretching	1649	1618	1589, 1535	1617,1566
C=C(phenyl) stretching	1596	1591	1480	1499
C-O	1307,1255	1332,1290	1313,1240	1268,1230
C-N stretching	1217,1179, 1143	1264, 1220, 1161	1174,1115	1172,1141
N-N hydrazine stretching	1112	1104	1170	1168

compound **1** absorbs at 376 nm and compound **2** absorbs at 350 nm. The close match between the theoretical predictions and the experimental observations validates these transitions.

3.3. *In vitro* antibacterial studies

The *in vitro* antibacterial activity of the synthesized hydrazones was assessed against a Gram-positive bacterium (*S. aureus*) and a Gram-negative bacterium (*E. coli*) using the well diffusion method. The antibacterial effectiveness, as measured by the diameter of the inhibition zones, is summarized in **Table S5**. According to the results the compounds **1** and **2** have the capability to act as effective antibacterial agent against *S.aureus*. The compounds shown significant growth-inhibitory potency. As the concentration of the chemical increased, the zone of inhibition expanded proportionally, indicating that higher chemical concentrations more effectively inhibit bacterial growth. Compound 1 possess slightly better activity against S. aureus since it showed a diameter zone of 17 mm with concentration 3mg/mL whereas that of

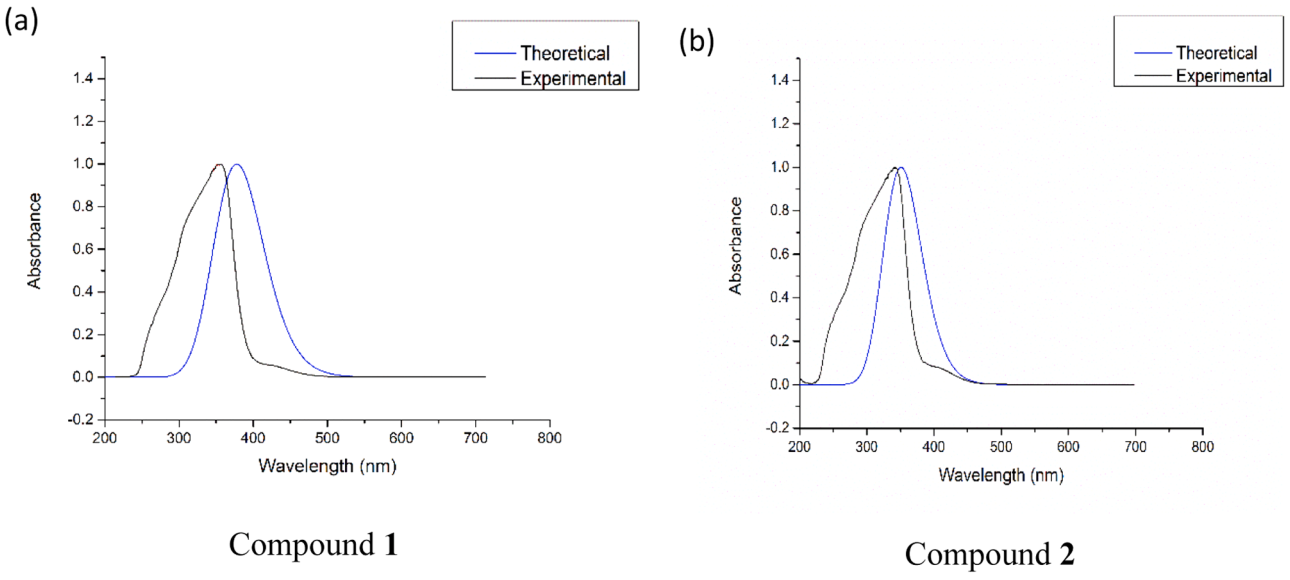

Fig. 13. Experimental and theoretical electronic spectra of compound 1 and 2.

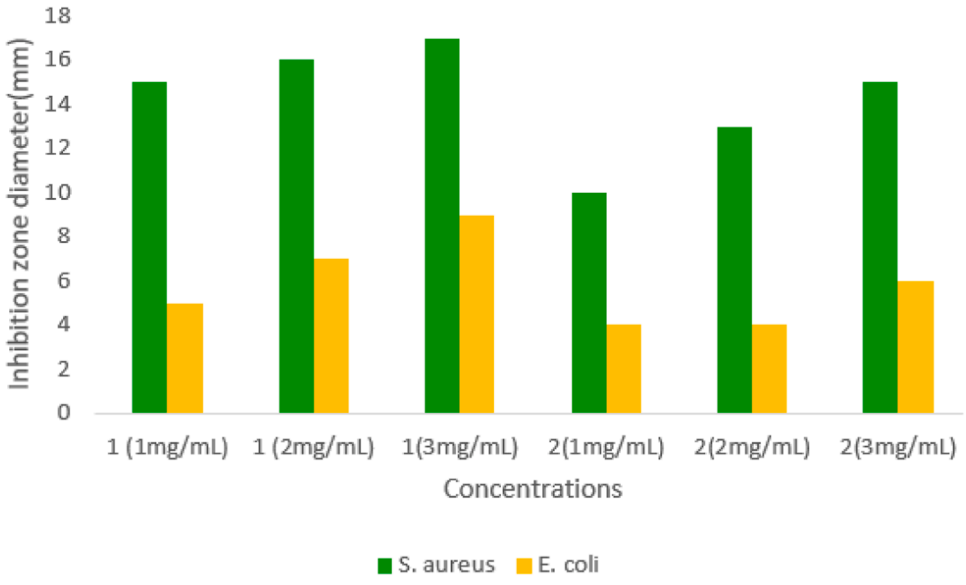

Fig. 14. Graphical representation of the antibacterial activity of aroylhydrazones against *S. aureus* and *E. coli*.

compound 2 was 15 mm (**Fig. S4**). The antibacterial activity of the synthesized aroylhydrazones against test organisms is depicted graphically in Fig. 14.

3.4. Molecular docking analysis

Molecular docking is a computer approach that predicts how small compounds, such as medications or inhibitors, would attach to a certain protein. Molecular docking involves modelling the interaction between a ligand (a small molecule) and a receptor (a protein) to predict the optimal binding conformation and affinity, making it an effective method for understanding ligand-protein interactions in pharmaceutical design. The *in vitro* antibacterial study revealed that compounds **1** and **2** displayed the strongest antibacterial activity, as indicated by the largest zone of inhibition, against S. aureus. Molecular docking studies were done to explain the promising *in vitro* findings for the hydrazones with four different proteins of *S. aureus* (**Table S4**). It provides the optimum position in connection with the target protein. The stability of the protein-ligand complex is assessed by examining both the highest binding energy and the number of ligand-active site residues. During docking into the active site, ligands can primarily interact via hydrogen bonding, Van der Waals, electrostatic, and hydrophobic interactions. Literature indicates that in order to anticipate the optimal binding mode, binding energy is a more important factor than the number of interactions. From the data on binding energy and interactions with the proteins, it is evident that both hydrazones exhibit a higher binding affinity for the protein dehydrosqualene synthase (CrtM) (PDB ID: 2ZCO).

Dehydrosqualene synthase is an enzyme that catalyzes the formation of dehydrosqualene from farnesyl pyrophosphate, a key step in the biosynthesis of carotenoids such as staphyloxanthin, which is important for the virulence of *S. aureus*. The primary function of the pigment is to act as an antioxidant, protecting S. aureus from oxidative stress caused by host immunological defence mechanisms including reactive oxygen species and neutrophils [57]. Compound 1 demonstrates binding affinities of −8.0, −8.3, −8.0, and −9.2 kcal/mol for the target proteins 5IIP, 6FXP, BOE, and 2ZCO from S. aureus, respectively. In comparison, compound 2 exhibits binding affinities of −8.3, −7.8, −7.7, and −9.1 kcal/mol for these same proteins. Both the hydrazones show highest binding affinity towards 2ZCO and are found to bind within the same binding pocket (Fig. 15) of coordinate (56,11,53) with cavity volume 2489 $Å^3$ of 2ZCO. The binding interactions of the studied molecules with receptor 2ZCO are depicted in detail in **Fig. S5** and **S6**. Several non-bonding interactions were identified in both the 1–2ZCO and 2–2ZCO complexes (Table 4). In compound **2** two conventional hydrogen bonds with distance 2.27 Å and 2.39 Å are observed. One of the hydrogen bonds is formed between the nitrogen atom of the NH group of **2** with GLN165 and the second hydrogen bond is formed between –NH groups ARG45 with oxygen of the O=C group of **2**. Whereas in compound **1** the conventional hydrogen bonds are absent. In compound **2** pi-anion and pi-sigma bonds are observed with ASP45 and PHE22. LEU164, VAL137, ALA134 and VAL133 amino acid residues present in 2ZCO interacted by means of pi-alkyl bonds. Carbon-hydrogen bond is also observed with HIS18. The significant non-bonding interaction of **1** with 2ZCO are pi-sigma bond with LEUA160 and pi-alkyl bonds with ALA157, LEU141, GLY161, LEU164, ALA134, VAL137 and HIS18. With GLY161 Carbon-hydrogen bond is also present. Based on interactions and binding energy, it may be inferred that both **1** and **2** have a higher binding energy in site 1 of the protein target 2ZCO. Surface structure of compound **1** and **2** with 2ZCO is represented in Fig. 16. Thus, the observed inhibition of S. aureus by compounds **1** and **2** may be due to their effect on the Dehydrosqualene synthase enzyme. This suggests that deactivation of this enzyme is a key component of their antibacterial activity.

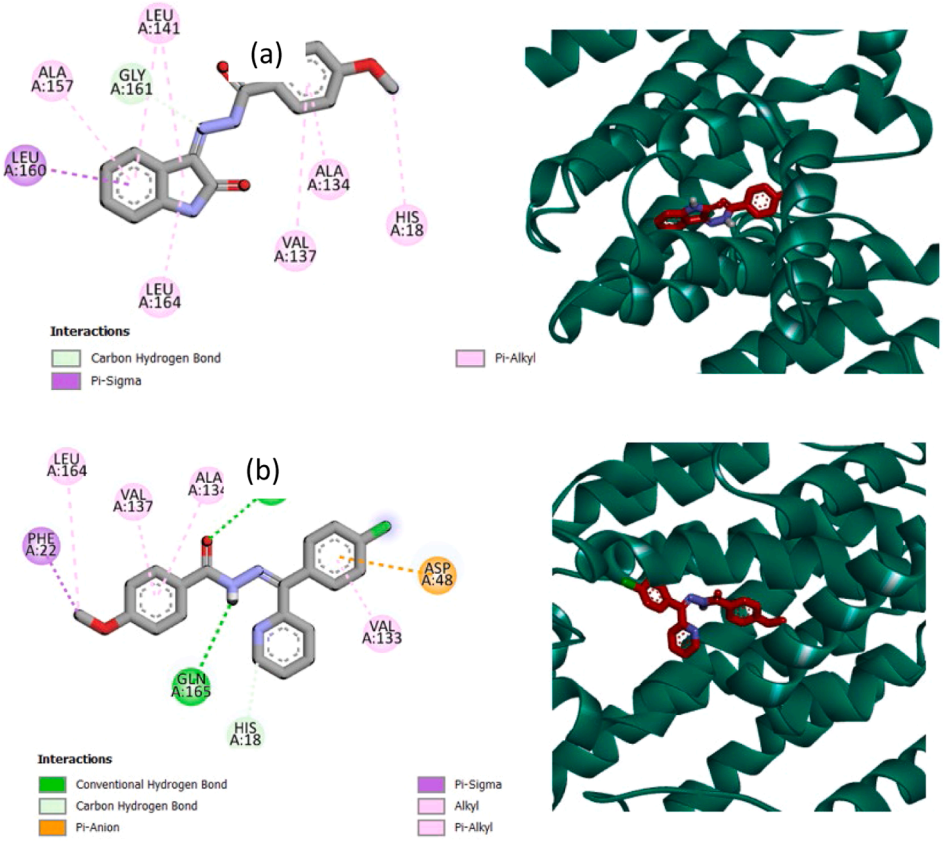

Fig. 15. Two-dimensional and three-dimensional structures of 2ZCO with Compound 1(a) and 2 (b).

Table 4
Interactions of hydrazones with the amino acid residues of the target protein 2ZCO in *S.aureus*.

Ligand	Active target	Active site	BE Kcal/mol	Interactions with amino acid residue		
				Vander Waals	**H-Bond**	**Hydrophobic**
1	2ZCO	1	−9.2	GLY138, VAL133, GLN45, ASN168, PHE22, TYR248, TYR41, LEU145, PHE261, ILE241	0	GLY161, (C-H), LEU160 (Pi-sigma), ALA157, LEU141, LEU164, VAL137, ALA134, HIS18, (Pi-alkyl)
2	2ZCO	1	−9.1	CYS44, GLY161, ASN168, TYR129, VAL111, TYR41	GLN165 (2.39 Å), ARG45 (2.27 Å)	ASPA48 (Pi-anion) PHE22 (Pi-sigma), HIS18 (C-H), VAL137, ALA134, VAL133, LEU164(Pi-alkyl)

3.5. ADME analysis

ADME analysis, which examines a drug's absorption, distribution, metabolism, and excretion in a biological system, is crucial in drug development and pharmacokinetics for optimizing effectiveness and minimizing potential side effects. The pharmacokinetic characteristics of the synthesized hydrazones were computed using SWISSADME in order to analyse the ADME properties of these compounds. This website allows you to figure out physicochemical descriptors and estimate ADME parameters, druglike nature, pharmacokinetic characteristics, and pharmacological compatibility of small compounds to aid in drug discovery. The obtained parameters are shown in Table 5. Lipinski's rule illustrates molecular features rather than pharmacological activity [58]. According to this rule, a drug has strong oral action if it has not more than one violation of the following criteria. 1. Molecular weight (MW) less than 500, 2. Octanol-water partition coefficient (log P) < 5, 3. The total number of NH and OH bonds < 5 hydrogen bond donors, 4. A total of less than ten hydrogen bond acceptors (N and O atoms), 5. The molar refractivity ranges from 40 to 130. From the table it is clear that both of the hydrazones are not showing any violation indicating the possibility of these substances acting as oral active drug. Assessment of drug-likeness was analysed by bioavaliability radar (Fig. 17), which indicates six physicochemical properties such as size, lipophilicity, solubility, polarity, flexibility and saturation.

3.6. Conclusion

The condensation reaction of 4-methoxybenzhydrazide with 1H-Indole-2,3-dione and 2-(4-chloro) benzoyl pyridine yielded two new aroylhydrazones,1H-Indole-2,3-dione 4-methoxybenzhydrazone and 2-(4-chloro) benzoyl pyridine 4-methoxybenzhydrazone. The structures of the newly synthesized compounds were confirmed through physicochemical analyses. Differently substituted hydrazones change hydrogen bonding patterns, thereby impacting intermolecular forces, molecular packing, and the overall supramolecular structure. DFT studies provide valuable insights into the molecular geometry and electronic structure of the investigated compounds. While some deviations from the crystal structure parameters are observed, these differences are attributed to intermolecular interactions present in the solid state. Anti-bacterial data suggest that the studied compounds could serve as effective inhibitors against Gram-positive bacteria. Furthermore, molecular docking calculations provided deeper insights, revealing that one of these compounds demonstrates a significantly stronger binding affinity to the target bacterial enzymes, which correlates with its enhanced biological activity. This combination of experimental and computational evidence highlights the potential of the compound as a potent antibacterial agent.

CRediT authorship contribution statement

Reshma P . R . : Writing – original draft. **Lincy Tom:** Writing – original draft. **Dhanya N . P . :** Software. **K.P. Safna Hussan:** Software, Formal analysis. **Vinod P. Raphael:** Formal analysis. **V.B. Bhagyesh:** Formal analysis. **Bibitha Joseph:** Supervision.

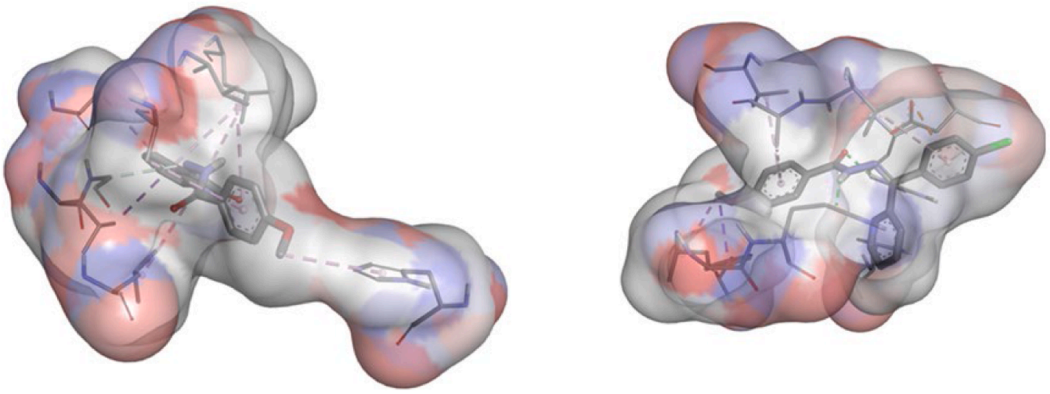

Fig. 16. Surface structure of compound 1 and 2 with 2ZCO.

Table 5
Lipinski rule of five-In silico physicochemical and pharmacokinetic parameters of the synthesized hydrazones.

Compound	log P <5	MW <500g/mol	H-Bond acceptor <10	H-Bond donor <5	n-rot	TPSA (°A)	Molar refractivity 40–130
1	1.80	295.29	4	2	4	79.79	84.43
2	3.67	365.81	4	1	6	63.58	101.39

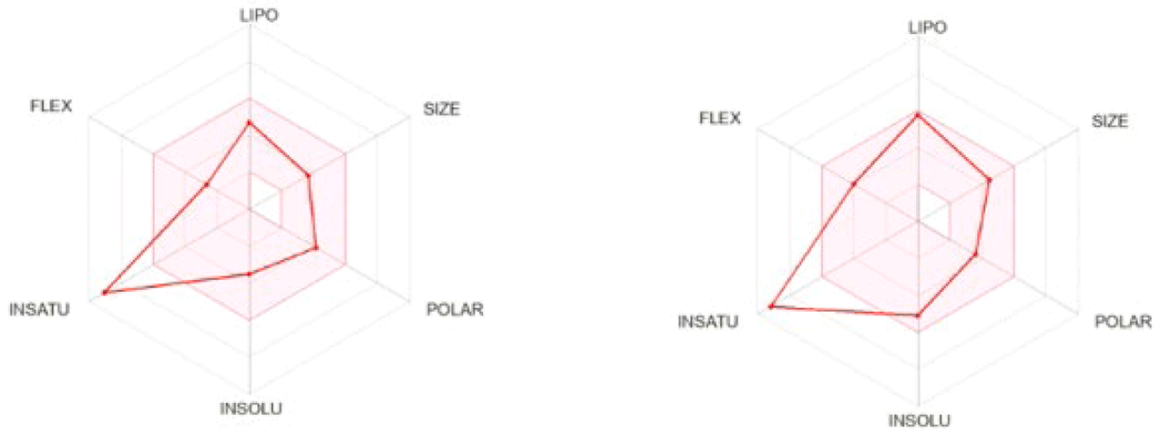

Fig. 17. Bioavaliability radar of compound 1 and compound 2.

Declaration of competing interest

The authors declare no conflict of interest.

Acknowledgements

Bibitha Joseph and P.R. Reshma acknowledge DST-FIST (SR/FST/College-001/2009(c) and SR/FST/COLLEGE/2023/1354), DST-CURIE (DST/CURIE-PG/2023/33) and KSCSTE-SARD (KSCSTE/623/2019-SARD) support to St Joseph's College (Autonomous), Irinjalakuda. The authors are grateful to SAIF, Cochin University of Science and Technology, Kochi, Kerala, India for elemental analysis and Single Crystal X-ray diffraction studies.

Appendix A. Supplementary data

CCDC 2351264 and 2351266 contains the supplementary crystallographic data for compounds **1** and **2** respectively. Copies of this information may be obtained free of charge via www.ccdc.cam.ac.uk/conts/retrieving.html or from the Director, CCDC, 12 Union Road, Cambridge, CB2, IEZ, UK (fax: +44-1223-336-033; e-mail: deposit@ccdc.cam.ac.uk).

Supplementary materials

Supplementary material associated with this article can be found, in the online version, at doi:10.1016/j.molstruc.2025.141866.

Data availability

Data will be made available on request.

References

[1] J. Chakraborty, S. Thakurta, G. Pilet, D. Luneau, S. Mitra, Polyhedron 28 (2009) 819, https://doi.org/10.1016/j.poly.2008.12.018.
[2] C. Wang, N. Xing, W. Feng, S. Guo, M. Liu, Y. Xu, Z. You, Inorg. Chim. Acta 486 (2019) 625, https://doi.org/10.1016/j.ica.2018.11.020.
[3] Y. Shibuya, K. Nabari, M. Kondo, S. Yasue, K. Maeeda, F. Uchida, H. Kawaguchi, Chem. Lett. 37 (2008) 78, https://doi.org/10.1246/cl.2008.78.
[4] A. Tabbiche, A. Bouchama, N. Chafai, F. Zaidi, C. Chiter, M. Yahiaoui, A. Abiza, J. Mol. Struct. 1261 (2022) 132865, https://doi.org/10.1016/j.molstruc.2022.132865.
[5] A.C. Day, M.C. Whiting, Org. Synth. 6 (1970) 10.
[6] W. Cao, Y. Liu, T. Zhang, J. Jia, Polyhedron 147 (2018) 62, https://doi.org/10.1016/j.poly.2018.03.012.
[7] M. Bagherzadeh, M.M. Haghdoost, A. Ghanbarpour, M. Amini, H.R. Khavasi, E. Payab, A. Ellern, L.K. Woo, Inorg. Chim. Acta 411 (2014) 61, https://doi.org/10.1016/j.ica.2013.11.026.
[8] A. Sanam, N. Nader, S.S. Mirabdullah, M. Kheirollah, F. Nazanin, Polyhedron 160 (2019) 115, https://doi.org/10.1016/j.poly.2018.12.023.
[9] A.A.A. Abu-Hussen, J. Coord. Chem 59 (2006) 157, https://doi.org/10.1071/CH06025.
[10] Y. Li, Z. Yang, Z.M. Zhou, Y. Li, J. He, X. Wang, Z. Lin, RSC Adv. 7 (2017) 41527, https://doi.org/10.1039/C7RA05504H.
[11] R. Eswaran, G. Valentina, B. Roberta, S. Paolo, N. Karuppannan, S.P.B. Nattamai, V. Alfonso, Z. Alfonso, G. Antonella, D. Alessandro, A. Alberto, M. Cristina Marzano, J. Inorg. Biochem. 182 (2018) 18, https://doi.org/10.1016/j.jinorgbio.2018.01.016.
[12] D. Kaushik, S.A. Khan, G. Chawla, S. Kumar, Eur. J. Med. Chem. 45 (2010) 3943, https://doi.org/10.1016/j.ejmech.2010.05.049.
[13] S.Y. Ebrahimipour, I. Sheikhshoaie, J. Simpson, H. Ebrahimnejad, M. Dusek, N. Kharazmi, V. Eigner, New J. Chem. 40 (2016) 2401, https://doi.org/10.1039/C5NJ02594J.
[14] L. Tom, C.R. Nirmal, A. Dusthackeer, B. Magizhaveni, M.R.P. Kurup, New J. Chem. 44 (2020) 4467, https://doi.org/10.1039/C9NJ06351J.
[15] D. Kuriakose, A.A. Aravindakshan, M.R.P. Kurup, Polyhedron 127 (2017) 84, https://doi.org/10.1016/j.poly.2017.01.041.
[16] A.M. Elseman, D.A. Rayan, M.M. Rashad, J Mater. Sci.-Mater. Electron 27 (2016) 2652, https://doi.org/10.1007/s10854-015-4073-1.
[17] K. Li, Y. Xiang, X. Wang, J. Li, R. Hu, A. Tong, B.Z. Tang, J. Am. Chem. Soc. 136 (2014) 1643, https://doi.org/10.1021/ja411689w.
[18] S.Y. Sheikhshoaie, M. Ebrahimipour, H.A. Sheikhshoaie, M. Rudbari, G. Bruno Khaleghi, Spectrochim. Acta 124A (2014) 548, https://doi.org/10.1016/j.saa.2014.01.043.
[19] L. Tom, M.R.P. Kurup, J. Mater. Chem. C 8 (2020) 2525, https://doi.org/10.1039/C9TC06710H.
[20] M. Maiti, S. Thakurta, G. Pilet, A. Bauzá, A. Frontera, J. Mol. Struct. 1226 (2021) 129346, https://doi.org/10.1016/j.molstruc.2020.129346.
[21] M.M. Fousiamol, M. Sithambaresan, V.A. Smolenski, J.P. Jasinski, M.R.P. Kurup, Polyhedron 141 (2018) 60, https://doi.org/10.1016/j.poly.2017.11.024.
[22] A.A. Aravindakshan, B. Joseph, U.L. Kala, M.R.P. Kurup, Polyhedron 123 (2017) 206, https://doi.org/10.1016/j.poly.2016.11.033.
[23] B. Jeragh, M.S. Ali, A.A. El-Asmy, Spectrochim. Acta, Part A 145 (2015) 295, https://doi.org/10.1016/j.saa.2015.03.021.
[24] T.R. Barman, M. Sutradhar, M.G.B. Drew, E. Rentschler, Polyhedron 51 (2013) 192, https://doi.org/10.1016/j.poly.2013.01.001.
[25] M. Sutradhar, L.M. Carrella, E. Rentschler, Eur. J. Inorg.Chem. 27 (2012) 4273, https://doi.org/10.1002/ejic.201200396.
[26] G. Rajmohan, R. Shanmugam, A. Elangovan, R. Sankaranarayanan, G. Ravindran, P. Dineshkumar, G. Arivazhagan, J. Mol. Struct. 1251 (2022) 132028, https://doi.org/10.1016/j.molstruc.2021.132028.
[27] M. Krishna Priya, B.K. Revathi, V. Renuka, S. Sathya, P. Samuel Asirvatham, Mater. Today Proc. 8 (2019) 37, https://doi.org/10.1016/j.matpr.2019.02.078.
[28] Y. Zhu, C.K. Xia, S.C. Meng, J. Chen, J. Chen, J.M. Xie, Polyhedron 61 (2013) 181, https://doi.org/10.1016/j.poly.2013.05.041.
[29] G. Ting, L. Hongzhi, L. Wenze, L. Lin, F. Chao, L. Hui, H.H. Li, L. Yinghua, S. A. Zhong-Min, J. Chem. Inform. 8 (2016) 24, https://doi.org/10.1186/s13321-016-0133-7.
[30] M. Ahmad, H. Pervez, S. Zaib, M. Yaqub, M.M. Naseer, S.U. Khan, J. Iqbal, RSC Adv 6 (2016) 60826, https://doi.org/10.1039/C6RA10043K.
[31] S. Naseem, M. Khalid, M.N. Tahir, M.A. Halim, A.A.C. Braga, M.M. Naseer, Z. Shafiq, J. Mol. Struct. 1143 (2017) 235, https://doi.org/10.1016/j.molstruc.2017.04.093.
[32] A. Thirugnanasundar, M.P. Kesavan, S.M. Kumar, L. Ravi, R. Bhaskar, G. Rajagopal, J. Rajesh, Inorg. Chim Acta 526 (2021) 120543, https://doi.org/10.1016/j.ica.2021.120543.
[33] M. Hagar, H.A. Ahmed, G. Aljohani, O.A. Alhaddad, Int. J. Mol. Sci. 21 (2020) 3922, https://doi.org/10.3390/ijms21113922.
[34] S. Gatfaoui, A. Sagaama, N. Issaoui, T. Roisnel, H. Marouani, Solid State Sci 106 (2020) 101606, https://doi.org/10.1016/j.solidstatesciences.2020.106326.

[35] D. Kuriakose, M.R.P. Kurup, J. Mol. Struct. (2020) 127467, https://doi.org/10.1016/j.molstruc.2019.127467.
[36] G.M. Sheldrick, Acta Cryst C71 (2015) 3, https://doi.org/10.1107/S2053229614024218.
[37] S. Weber, J. Appl. Crystallogr. 32 (1999) 1028, https://doi.org/10.1107/S0021889899009152.
[38] C.F. Macrae, I. Sovago, S.J. Cottrell, P.T.A. Galek, P. McCabe, E. Pidcock, M. Platings, G.P. Shields, J.S. Stevens, M. Towler, P.A. Wood, J. Appl. Cryst. 53 (2020) 226, https://doi.org/10.1107/S1600576719014092.
[39] O.V. Dolomanov, L.J. Bourhis, R.J. Gildea, J.A.K. Howard, H. Puschmann, J. Appl. Cryst. 42 (2009) 339, https://doi.org/10.1107/S0021889808042726.
[40] M.J. Frisch, G.W. Trucks, H.B. Schlegel, G.E. Scuseria, M.A. Robb, J.R. Cheeseman, G. Scalmani, et al., Gaussian 09, rev. D. 01, Gaussian Inc., Wallingford, CT, USA, 2009.
[41] J.T. Rives, W.L. Jorgensen, J. Chem. Theory Comput. 4 (2008) 297, https://doi.org/10.1021/ct700248k.
[42] P. Vennila, M. Govindaraju, G. Venkatesh, C. Kamal, J. Mol. Struc. 1111 (2016) 151, https://doi.org/10.1016/j.molstruc.2016.01.068.
[43] Roy Dennington, Todd A. Keith, John M. Millam, GaussView, Version 6, Semichem Inc., Shawnee Mission, KS, 2016.
[44] M.R. Zaidan, A. Noor Rain, A.R. Badrul, A. Adlin, A. Norazah, I. Zakiah, Trop. Biomed. 22 (2) (2005) 165, https://doi.org/10.1175/JTECH-1683.1.
[45] W. DeLano, PyMOL Mol. Graphic. Syst. (2002).
[46] Discovery Studio, Release 4.5, Accelerys Software Inc, San Diego, 2016.
[47] F.H. Al-Ostoot, D.V. Geetha, Y.H.E. Mohammed, P. Akhileshwari, M.A. Sridhar, S. A. Khanum, J. Mol. Struct. 1202 (2020) 127244, https://doi.org/10.1016/j.molstruc.2019.127244.
[48] R.G. Parr, L.v. Szentpaly, S. Liu, J. Am. Chem. Soc. 121 (1999) 1922, https://doi.org/10.1021/ja983494x.
[49] D. Roy, U. Sarkar, P. Chattaraj, A. Mitra, J. Padmanabhan, R. Parthasarathi, V. Subramanian, S. Van Damme, P. Bultinck, Mol. Divers. 10 (2006) 119, https://doi.org/10.1007/s11030-005-9009-x.
[50] Y.N. Mabkhot, F.D. Aldawsari, S.S. Al-Showiman, A. Barakat, S.M. Soliman, M. I. Choudhary, S. Yousuf, M.S. Mubarak, T.B. Hadda, Chem. Cent. J. 9 (2015) 1, https://doi.org/10.1186/s13065-015-0100-9.
[51] E.B. Sas, M. Kurt, M. Can, N. Horzum, A. Atac, J. Mol. Struct. 1118 (2016) 124, https://doi.org/10.1016/j.molstruc.2016.03.064.
[52] S.I. Levchenkov, V.V. Lukov, V.A. Kogan, L.D. Popov, I.N. Shcherbakov, Russ. J. Inorg. Chem., 38, 10, B. Bleaney, K.D. Bowers, Proc. R. Soc. London, Ser. A 214 (451) (1952) 1687.
[53] S. Naseem, M. Khalid, M.N. Tahir, M.A. Halim, A.A. Braga, M.M. Naseer, Z. Shafiq, J. Mol. Struct. 1143 (2017) 235, https://doi.org/10.1016/j.molstruc.2017.04.093.
[54] N. Sundaraganesan, H. Umamaheswari, B. Dominic Joshua, C. Meganathan, M. Ramalingam, J. Mol. Struct.: Theochem. 850 (2008) 84, https://doi.org/10.1016/j.theochem.2007.10.031.
[55] S. Bayarı, S. Saglam, H.F. Ustundag, J. Mol. Struct.: Theochem. 726 (2005) 225, https://doi.org/10.1016/j.theochem.2005.02.078.
[56] K. Chandrasekaran, R.Thilak Kumar, Spectrochim. Acta, Part A: Mol. Biomol. Spectros. 150 (2015) 974, https://doi.org/10.1016/j.saa.2015.06.018.
[57] Zheng Guan, Yafeng Song, Marcel de Vries, Hjalmar Permentier, Pieter Tepper, Ronald van Merkerk, Rita Setroikromo, Wim J. Quax, J. Agric. Food Chem. Calicut Univ. 72 (2024) 3017, https://doi.org/10.1021/acs.jafc.3c05770.
[58] C.A. Lipinski, Drug Discov. Today Technol 4 (2004) 337, https://doi.org/10.1016/j.ddtec.2004.11.007.